Probing ionospheric structures using the LOFAR radio telescope

Article (Published Version)

AGU PUBLICATIONS

Radio Science

RESEARCH ARTICLE
10.1002/2016RS006028

Probing ionospheric structures using the LOFAR radio telescope

M. Mevius[1], S. van der Tol[1], V. N. Pandey[1], H. K. Vedantham[1,2], M. A. Brentjens[1], A. G. de Bruyn[1,2], F. B. Abdalla[3,4], K. M. B. Asad[2], J. D. Bregman[1], W. N. Brouw[1,2], S. Bus[2], E. Chapman[3], B. Ciardi[5], E. R. Fernandez[2], A. Ghosh[2], G. Harker[3], I. T. Iliev[6], V. Jelić[1,2,7], S. Kazemi[8], L. V. E. Koopmans[2], J. E. Noordam[1], A. R. Offringa[1], A. H. Patil[2], R. J. van Weeren[9], S. Wijnholds[1], S. Yatawatta[1], and S. Zaroubi[2]

[1]Astron, Dwingeloo, Netherlands, [2]Kapteyn Astronomical Institute, University of Groningen, Groningen, Netherlands, [3]Department of Physics and Astronomy, University College London, London, UK, [4]SKA, Pinelands, South Africa, [5]Max-Planck Institute for Astrophysics, München, Germany, [6]Astronomy Centre, Department of Physics and Astronomy, Pevensey II Building, University of Sussex, Brighton, UK, [7]Ruđer Bošković Institute, Zagreb, Croatia, [8]ASTRON and IBM Center for Exascale technology, Dwingeloo, Netherlands, [9]Harvard-Smithsonian Center for Astrophysics, Cambridge, Massachusetts, USA

Key Points:
- LOFAR is able to measure differential TEC values with an accuracy better than 1 mTECU
- The diffractive scale is an easily obtained single number indicating the ionospheric quality of a radio interferometric observation
- The ionospheric phase structure functions of most nights show a spatial anisotropy that is in many cases Earth magnetic field aligned

Correspondence to:
M. Mevius,
mevius@astron.nl

Citation:
Mevius, M., et al. (2016), Probing ionospheric structures using the LOFAR radio telescope, *Radio Sci.*, *51*, 927–941, doi:10.1002/2016RS006028.

Received 24 MAR 2016
Accepted 12 JUN 2016
Accepted article online 18 JUN 2016
Published online 12 JUL 2016

Abstract LOFAR is the LOw-Frequency Radio interferometer ARray located at midlatitude (52°53′N). Here we present results on ionospheric structures derived from 29 LOFAR nighttime observations during the winters of 2012/2013 and 2013/2014. We show that LOFAR is able to determine differential ionospheric total electron content values with an accuracy better than 0.001 total electron content unit = 10^{16}m^{-2} over distances ranging between 1 and 100 km. For all observations the power law behavior of the phase structure function is confirmed over a long range of baseline lengths, between 1 and 80 km, with a slope that is, in general, larger than the 5/3 expected for pure Kolmogorov turbulence. The measured average slope is 1.89 with a one standard deviation spread of 0.1. The diffractive scale, i.e., the length scale where the phase variance is 1 rad^2, is shown to be an easily obtained single number that represents the ionospheric *quality* of a radio interferometric observation. A small diffractive scale is equivalent to high phase variability over the field of view as well as a short time coherence of the signal, which limits calibration and imaging quality. For the studied observations the diffractive scales at 150 MHz vary between 3.5 and 30 km. A diffractive scale above 5 km, pertinent to about 90% of the observations, is considered sufficient for the high dynamic range imaging needed for the LOFAR epoch of reionization project. For most nights the ionospheric irregularities were anisotropic, with the structures being aligned with the Earth magnetic field in about 60% of the observations.

1. Introduction

With the arrival of long baseline radio interferometric arrays such as LOw-Frequency Radio interferometer ARray (LOFAR) [*van Haarlem et al.*, 2013], low-frequency radio astronomy has reached a new era. In radio astronomy low frequency refers to frequencies between a few tens of megahertz and a few hundred megahertz. LOFAR operates between 30 and 250 MHz. One of the scientific cases for LOFAR is the measurement of the redshifted 21 cm emission line of neutral hydrogen from the epoch of reionization (EoR) [*van Haarlem et al.*, 2013]. This EoR signal is expected to lie many orders of magnitude below the foreground astrophysical emission in a single observation. Thus, high dynamic range imaging is needed to extract the EoR signal. The required precision poses new challenges in calibration and imaging of the data. Ionospheric propagation delays are a major contributor to phase errors at low radio frequencies. Residual effects in the data due to ionospheric phase errors on the bright astrophysical foreground emission can pose a significant challenge to EoR experiments. It is for these reasons that we started a program to investigate the ionospheric disturbance in the LOFAR EoR observations. While the main goal of such a program is to remove the effects of the ionosphere, investigating the ionospheric phases also reveals a wealth of information on physical processes in the ionosphere, which is interesting in its own right. In addition, knowledge of the characteristics of the ionosphere gives improved estimates of the residual ionospheric *speckle noise* in the radio interferometric images after calibration [*Koopmans*, 2010; *Vedantham and Koopmans*, 2015]. In this paper we focus on the ionospheric

information extracted from LOFAR EoR calibration data that is relevant for assigning an ionospheric *quality* to a given radio interferometric observation.

An electromagnetic signal with frequency ν passing through the ionosphere undergoes an additional phase shift that is to first order equal to

$$\Delta\phi = -8.45 \left(\frac{\mathrm{TEC}}{1\ \mathrm{TECU}}\right) \left(\frac{\nu}{1\ \mathrm{GHz}}\right)^{-1} \mathrm{rad} \quad (1)$$

where TEC is the integrated electron density along the line of sight in TEC units and 1 TECU $= 10^{16}\mathrm{m}^{-2}$. The above equation is only valid for observing frequencies well above the maximum plasma frequency ($\approx$10 MHz). From the spectral dependence in equation (1) it is clear why the ionosphere is a major source of calibration errors especially at low frequencies. An interferometer only measures phase differences; therefore, to first order, its signal is only distorted if the ionospheric electron column densities above the two elements of an interferometer differ. Early experiments have shown that the ionosphere can be considered as a turbulent medium with scales over a long range of distances [*Wheelon*, 2001]. Consequently, the variance of the differential TEC is expected to follow a power law with the distance between two points in the ionosphere. It is the purpose of this paper to study this power law behavior and its slope over the long range of distances defined by the available baseline lengths of the Dutch LOFAR stations.

Ionospheric phases can be partly removed from the data using self-calibration [*Pearson and ReadHead*, 1984]. In self-calibration, a model of the sky and the instrument is used to predict the radio interferometric visibilities. Calibration parameters, including both amplitude and phase corrections for each element, are then determined by fitting the predicted visibilities to the data. The sky model is updated in an iterative sequence. Traditional self-calibration uses a single set of parameters for all directions and does not take into account the angular variation in ionospheric distortions over the field of view. Direction-dependent calibration [*Smirnov*, 2011] can take care of this, but it needs a good model of the radio sky, and it can only be done for a limited number of directions. Methods to interpolate between the direction-dependent ionospheric parameters and subsequently apply them in other directions are, for example, field-based calibration [*Cotton et al.*, 2004] or Source Peeling and Atmospheric Modeling (SPAM) [*Intema et al.*, 2009]. In self-calibration the sky model is extracted from the data themselves. For a high-resolution sky model, the longest baselines are needed, which suffer most from ionospheric distortions. In effect, residual ionospheric phase noise is inevitable, and good knowledge of the structure of the ionosphere helps in understanding this source of stochastic errors.

Most of our knowledge of the large-scale ionosphere is derived from measurements from dedicated experiments with ionosondes and GPS satellites and receivers. Measurements of ionospheric structure have been done by radio telescopes before, for example, traveling ionospheric disturbances (TIDs) [*van Velthoven*, 1990; *Spoelstra*, 1997; *Helmboldt et al.*, 2012], turbulent like fluctuations [*Spoelstra*, 1997; *Cohen and Röttgering*, 2009] and plasmaspheric irregularities [*Jacobson and Erickson*, 1992; *Helmboldt et al.*, 2012; *Loi et al.*, 2015]. LOFAR can contribute to these measurements in a unique way. The wide bandwidth of LOFAR observations in both its low band (30–80 MHz) and high band (110–190 MHz) observing mode allows good separation of the ionospheric effects from other errors that have a different frequency dependence. Also, the LOFAR layout facilitates probing ionospheric structures on a large range of scales. The dense inner core gives an instantaneous imprint of the small-scale structures ($\sim$2 km), whereas with the remote stations, LOFAR is sensitive to ionospheric structures up to 100 km in size. LOFAR also has stations in Germany, the UK, France, Sweden, and recently added Poland, building up baselines of more than 1000 km. Apart from exploiting LOFAR's array layout, its wide field of view and the simultaneous multibeaming capability facilitates studies of ionospheric structures over a large range of spatial scales in a complementary way. In this case, the phase distortions are not measured toward a single source but toward a large number of sources distributed over the large field of view of one or many simultaneous beams.

In this paper we will exploit LOFAR's phase solutions in the direction of a single bright and dominant calibrator to probe ionospheric structures on spatial scales corresponding to LOFAR's baselines, where we restrict ourselves to data from *Dutch* LOFAR. We thus use the results of traditional self-calibration in a single direction. The many-source approach will be the topic of a subsequent paper. We will globally discuss the effect of ionosphere on the quality of radio interferometric images. The diffractive scale is introduced as a single number representation of the ionospheric quality of an observation. A more quantitative approach using the diffractive scale to decide on calibration strategies will be left for future work.

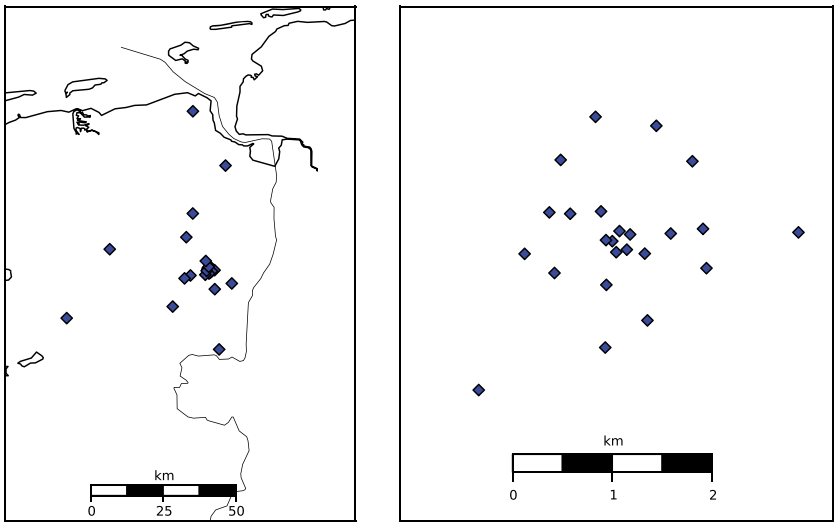

Figure 1. Layout of the LOFAR Stations. (left) All Dutch stations. (right) The central core of LOFAR.

In section 2 we will discuss our data set, and in section 3 we outline how we collected ionospheric information from self calibration solutions. Section 4 deals with the framework of ionospheric spatial variability. The two-dimensional structure function will be introduced here. In section 5 the result of fitting this ionospheric structure function on data of many nights is shown, and the ionospheric phase structure function will be correlated with image noise. Here we will also discuss anisotropy and elongation of structures along the magnetic field lines, which has been observed for many nights. Discussion of the results will follow in section 6.

2. Data Description

The center of LOFAR is located in the Netherlands at midlatitude (52°53′N, 6° 52′E). The analysis in this paper is performed using data between 110 and 190 MHz from LOFAR's High Band Antennas (HBA). It uses all baselines formed from LOFAR's core and remote stations, giving projected baselines ranging from 30 m to 100 km. The LOFAR core HBA stations are arranged in two fields each with a diameter of 31 m. For the EOR observations these are treated as individual stations at the correlator, resulting in a total of 48 core stations, of which 46 were used in the analysis. The number of remote stations at the time of observations was 13 for most, the fourteenth station was added during 2013. The full width at half maximum of the stations varies between 4.8 and 3.2° in the given frequency range. Figure 1 shows the layouts of all Dutch LOFAR stations and the LOFAR core.

For our analysis we used many nights with data collected for the epoch of reionization project. In the LOFAR-EoR project the data of several hundreds of hours of observations of the same field are combined to extract the signal. The two main fields that are being observed are one in the direction of the North Celestial Pole and the other with the phase center at the bright quasar 3C196 (J2000:RA 08h13m36s,Dec +48d13m03s). We chose the latter field for our analysis, since the bright calibrator in the center of the field eases the extraction of the ionospheric information. The EoR project requires nighttime observations. Therefore, in the current analysis, we only study nighttime characteristics of the ionosphere. Also, since 3C196 is only above the horizon during nighttime in the winter, our observations are restricted to these months.

We selected the first 29 observations of the 3C196 field. Of these, 26 were recorded in the winter of 2012/2013, the last three are from 2013/2014. Most of the observations last for 8 h, centered on the meridian transit of 3C196. There are also six 6 h observations. For comparison and to avoid systematic effects that are mainly present at low elevations, all results presented here use only the middle 6 h of the observations, unless specified otherwise. The exact epochs and durations of the observations are listed in Table 1.

The data consist of 380 subbands, each with a width of 195.3 kHz, covering the frequencies between 115 and 189 MHz. The raw data in each subband were recorded with an integration time of 2 s and 64 channels per subband (each with a width of about 3 kHz), which after flagging for radio frequency interference using the AOFlagger algorithm [*Offringa et al.*, 2010, 2012] were averaged to the final data product with a resolution of 10 s and 1 channel per subband. The first and last two channels of the original data were discarded, resulting

Table 1. Parameters of All Observations[a]

Id	Date	Start Time (UTC)	Length (Hour)	β	Major (km)	Minor (km)	r_{diff} (km)	σ (mTEC)	α	fa
L78444	2012/11/30	23:04:41	8	1.92 ± 0.04	12.8 ± 0.2	10.4 ± 0.7	11.4	1.00	147.0 ± 8.6	1.8
L79324	2012/12/06	22:41:05	8	1.88 ± 0.02	5.8 ± 0.2	3.6 ± 0.1	4.3	0.91	158.9 ± 1.9	3.2
L79344	2012/12/09	22:29:17	8	1.96 ± 0.02	13.8 ± 0.6	6.3 ± 0.2	8.7	1.05	118.8 ± 0.8	1.2
L80273	2012/12/12	22:17:30	8	1.98 ± 0.01	22.8 ± 0.5	9.3 ± 0.3	13.3	0.97	147.2 ± 1.1	2.3
L80508	2012/12/16	22:01:46	8	2.00 ± 0.01	23.1 ± 0.7	5.8 ± 0.2	9.3	1.04	101.3 ± 0.4	0.8
L80898	2012/12/19	21:49:58	8	1.67 ± 0.02	5.5 ± 0.2	2.8 ± 0.1	3.5	0.46	2.2 ± 1.4	5.8
L80897	2012/12/21	21:42:07	8	1.86 ± 0.03	25.3 ± 0.1	21.8 ± 1.5	23.4	1.41	43.6 ± 17.3	1.6
L80895	2012/12/28	21:14:35	8	1.62 ± 0.04	15.0 ± 0.1	4.2 ± 1.2	6.4	0.61	46.4 ± 0.8	4.3
L82609	2012/12/29	21:10:39	8	1.89 ± 0.01	33.7 ± 0.8	28.8 ± 0.6	31.1	1.01	1.5 ± 5.5	0.9
L82655	2013/01/01	20:58:51	8	1.98 ± 0.01	18.0 ± 0.4	9.5 ± 0.3	12.4	1.13	122.5 ± 1.9	1.5
L80893	2013/01/04	20:47:04	8	1.84 ± 0.04	6.1 ± 0.0	5.1 ± 0.2	5.5	1.24	70.4 ± 8.0	2.9
L80892	2013/01/09	20:27:24	8	1.94 ± 0.01	35.4 ± 1.1	23.9 ± 0.5	28.8	1.01	131.9 ± 3.5	1.1
L80891	2013/01/11	20:19:32	8	1.91 ± 0.02	7.8 ± 0.2	5.1 ± 0.1	6.2	1.23	115.5 ± 3.4	1.3
L83991	2013/01/18	19:52:01	8	1.84 ± 0.04	8.7 ± 0.5	3.1 ± 0.1	4.4	0.61	36.7 ± 0.7	2.7
L84999	2013/01/21	19:40:13	8	1.66 ± 0.03	19.2 ± 0.6	7.6 ± 0.4	10.9	0.72	148.8 ± 1.2	3.2
L85001	2013/01/26	19:20:33	8	1.97 ± 0.01	24.0 ± 0.6	7.5 ± 0.2	11.3	0.97	111.1 ± 1.3	1.3
L83988	2013/01/30	21:04:50	6	1.78 ± 0.03	12.2 ± 0.4	5.5 ± 0.4	7.4	1.12	150.4 ± 3.1	2.4
L83987	2013/02/01	18:56:58	8	1.88 ± 0.02	21.5 ± 0.5	12.5 ± 0.3	15.7	0.83	169.4 ± 2.5	4.2
L86767	2013/02/07	18:33:23	8	1.85 ± 0.02	8.3 ± 0.3	3.6 ± 0.1	4.8	0.95	14.8 ± 1.1	3.9
L86766	2013/02/08	18:29:27	8	2.00 ± 0.01	21.4 ± 0.4	12.5 ± 0.7	15.9	0.88	124.6 ± 4.0	1.6
L94157	2013/02/15	18:01:56	8	1.92 ± 0.01	24.6 ± 1.3	8.9 ± 0.2	12.8	0.86	176.2 ± 1.0	4.6
L95140	2013/02/22	17:34:24	8	1.96 ± 0.01	19.2 ± 1.0	11.9 ± 0.3	14.6	0.83	160.0 ± 4.0	2.1
L95139	2013/02/23	17:30:28	8	1.71 ± 0.03	16.9 ± 0.4	8.3 ± 0.4	11.0	0.71	158.9 ± 2.0	3.2
L98635	2013/03/03	16:59:01	8	1.88 ± 0.02	18.9 ± 0.6	9.2 ± 0.1	12.4	0.79	170.4 ± 1.0	2.9
L99279	2013/03/07	17:43:17	6	1.99 ± 0.01	19.7 ± 0.4	9.9 ± 0.2	12.8	0.77	21.4 ± 1.0	1.3
L99278	2013/03/08	17:39:21	6	2.01 ± 0.01	25.0 ± 1.1	12.6 ± 0.3	16.3	0.80	30.9 ± 0.6	0.9
L102492	2013/03/12	17:23:38	6	1.95 ± 0.02	16.3 ± 0.6	7.2 ± 0.4	9.9	0.81	171.1 ± 4.6	2.2
L192832	2013/12/15	23:06:38	6	1.95 ± 0.01	27.2 ± 0.4	17.6 ± 1.2	21.3	0.84	130.6 ± 2.4	2.2
L196869	2014/01/04	21:48:00	6	1.89 ± 0.02	17.2 ± 0.5	14.2 ± 0.3	15.6	0.86	93.9 ± 6.5	2.1

[a]In the last column (*fa*) the ratio of field aligned and field perpendicular r_{diff} is given.

in a width of 183.1 kHz per subband. After flagging and averaging, the data were calibrated with the LOFAR Blackboard Self calibration system [*Pandey et al.*, 2009]. During calibration, the complex gains are fitted by minimizing the difference between the recorded visibilities and the model visibilities. The model visibilities are generated using a model of the sky and the antenna pattern. The resulting calibration gains contain the effect of any distortions between the emitter and the antenna, among which are the residual unmodeled antenna gain pattern, instrumental errors, and atmospheric and ionospheric effects [*Smirnov*, 2011]. Our sky model consists solely of four components of the dominant source 3C196 (V. N. Pandey, private communication). We ignored the weaker sources in the field, since 3C196 is about 14 times brighter than the second brightest source. The effects of the *missing* sky in our model can be seen as a second-order effect in the phase solutions, which will be discussed in more detail in section 4. The effect of the primary beam was taken into account using the standard LOFAR beam model [*Pandey et al.*, 2009].

3. Obtaining Ionospheric Information From Calibration Phases

The main contribution of ionospheric propagation at LOFAR frequencies is a dispersive delay, showing up in the calibration phases. However, the interferometric calibration phases also contain other effects. In particular, since the remote stations are not on a common clock as the core, a main source of (time-varying) phase errors

are the drifting clock errors. The clock errors can be as large as 200 ns, with a drift rate in the order of $1e^{-12}$. Other, smaller, effects include cable reflections, beam model errors, tropospheric delay fluctuations, and the imperfect sky model.

It is possible to distinguish clock from ionospheric phases by using the wide frequency range and the difference in frequency behavior of the two effects. The phase error between station i and j is as follows:

$$\delta\phi_{ij}(\nu) = (2\pi \cdot \delta\tau_{ij} \cdot \nu - C_1 \cdot \delta\mathrm{TEC}_{ij}/\nu) \quad \mathrm{rad}, \tag{2}$$

where $C_1 \approx 8.45e^9 \mathrm{m}^2\mathrm{s}^{-1}$ is the ionospheric conversion, ν the signal frequency in hertz and $\delta\mathrm{TEC}_{ij}$ the difference in integrated ionospheric electron content in TECU between the line of sights to stations i and j. The relative timing error on the clocks at the stations i, j is $\delta\tau_{ij}$ (s). In order to extract the TEC information from the calibration phases, we selected the phase solutions of 31 subbands uniformly distributed over a 115–175 MHz range and fitted function (2) to the data. We limited the number of subbands used in our analysis to about 8% of the available data for reasons of computational cost. Because the final accuracy of the TEC values is limited by systematic errors, as will be shown in section 4, this has negligible influence on the accuracy of our results.

Since $\delta\phi_{ij}$ can only be measured up to a $n \cdot 2\pi$ ambiguity, the phase data were first unwrapped. Unwrapping can be done if the parameters $\delta\tau_{ij}$, and $\delta\mathrm{TEC}_{ij}$ are known to a reasonable precision a priori. Best initial estimates of $\delta\tau_{ij}$ and $\delta\mathrm{TEC}_{ij}$ were found for the first time slot of an observation by searching over a large range of possible solutions to find the best fitting match. For subsequent time slots the parameters were initialized with the solution of the previous time slot and the phases unwrapped accordingly before performing the fit. This is possible since we do not expect the station clocks and/or the differential TEC to vary substantially within a single time slot of 10 s. The accurate phases due to the high signal-to-noise ratio of the calibrator ensures that the solutions stay in the same local minimum (2π interval) over time. A full 2π phase wrap corresponds in the observed frequency range to a jump in the TEC and clock value of ~ 0.05 TECU and ~ 3 ns, respectively. No such jumps were found when checking the time variation of the fitted parameters. The maximum absolute difference between two time slots for all observations is 0.029TECU and 0.9ns for the TEC and clock solutions, where on average it is 0.0015 TECU and 0.05 ns for the longest baselines.

After an initial iteration of the clock/TEC separation fit, the time-averaged spatial correlation of differential TEC values was checked per observation by fitting a linear two-dimensional polynomial over the time-averaged TEC values projected on the positions of the different stations. Remaining 2π phase wraps (by construction constant over the full observation) could be detected this way as well as a small constant (both in frequency and time) phase offset per station. Such a phase offset is typically introduced by the station calibration solutions, which are applied on-the-fly to the data prior to interferometric correlation. After these corrections, final parameter values were determined in a second iteration of the clock/TEC separation. A typical example of the fitted differential TEC values is shown in Figure 2 both for the full array and for the core stations. The TEC values are shown with the central station CS001HBA0 as a reference. The color scale corresponds to baseline length. Temporal ionospheric variations that are spatially correlated from station to station are clearly observed even on the short (~ 1 km) baselines.

The accuracy of the TEC solutions that can be reached with this method is limited by ignoring second-order phase effects. Especially effects that are not linear in frequency, and thus cannot be absorbed in the clock solutions, will be partially absorbed in the TEC solutions. Examples of such phase errors are cable reflections, sky, and beam model errors.

4. Ionospheric Structure Function

The spatial structure of a medium like the ionosphere can be characterized by its power spectrum, or equivalently, its Fourier inverse—the phase correlation function. In practice, it is convenient to measure the spatial correlation in terms of the phase structure function [*van der Tol*, 2009], defined as follows:

$$D(r) = \left\langle \left(\phi(r') - \phi(r'+r)\right)^2 \right\rangle. \tag{3}$$

For Kolmogorov turbulence, the phase structure function takes the form of a power law in the inertial range of turbulence:

$$D(r) = \left(\frac{r}{r_{\mathrm{diff}}}\right)^{\beta}, \tag{4}$$

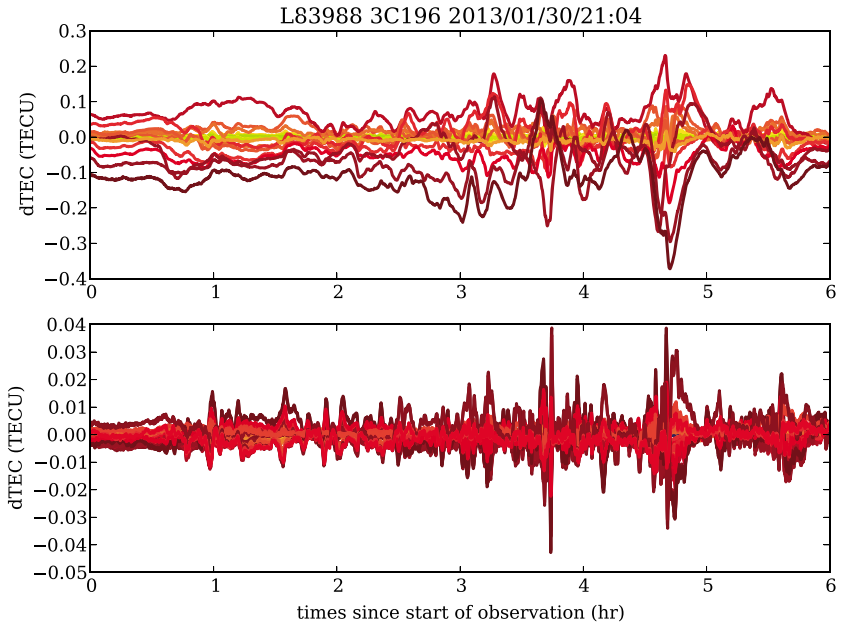

Figure 2. Differential TEC of LOFAR stations with respect to the central station versus time, single observation. The color coding is corresponds to the baseline length, with longer baselines having darker colors. (top) All stations. (bottom) Only core stations (maximum baseline 2 km).

where r_{diff} is the spatial scale over which the phase variance is 1 rad^2 and is referred to as the *diffractive scale* [*Narayan*, 1992]. The index β is equal to 5/3 for pure Kolmogorov turbulence.

In order to measure the structure function using the LOFAR data, we determine the variance per baseline of the differential TEC as shown in Figure 2. From Figure 2 it is clear that the time average of the differential TEC for two stations is not zero. In fact, there is a large north-south TEC gradient over the array that is visible in all observations and is merely a result of the very large scale global ionospheric structure. By calculating the phase variance, and thus using the mean subtracted values, we implicitly filter out this global structure. We converted the slant TEC (sTEC) values to vertical TEC (vTEC) by dividing with the slant factor, assuming a single layer ionosphere at 300 km, taking into account the zenith angle in the direction of the source. This correction factor is calculated as follows:

$$v\mathrm{TEC} = cos(\alpha') \cdot s\mathrm{TEC}, \quad \alpha' = a\sin\left(\frac{R_{\mathrm{Earth}}}{R_{\mathrm{Earth}} + h} \cdot \sin(\alpha)\right). \tag{5}$$

With R_{Earth} the Earth radius and h the altitude of the single layer approximation of the ionosphere and α the zenith angle. The dependence of this correction on the exact altitude of the single layer is minor.

The vertical differential TEC values were converted to a differential phase at 150 MHz for comparison with other experiments using equation (1). We use the time average of the phase variations to estimate the ensemble average. The observations are 6 h long, a timescale much longer than the coherence scale. In these 6 h we are tracking a source, corresponding to tracking the ionosphere over a projected distance of ∼300 km on an ionospheric layer at 300 km height. At the same time ionospheric structures are moving. TIDs, for example, are moving with a typical speed of a few hundred kilometers per hour. In general, this increases the size of the sampled space, although one should keep in mind that the propagation direction of the ionospheric structures could coincide with that of the source. For the reasons mentioned above, we sample enough independent data points on the ionospheric screen to allow the ergodic theorem to hold. An example of the unbinned spatial phase structure function of a typical observation, the same as used for Figure 2, is shown in Figure 3.

The figure shows some typical features. First, for a large range of baseline lengths, between 1 and 80 km, the power law behavior is apparent. There is a hint of a turnover at the very long baselines (∼80 km), which may represent the outer scale of turbulence at which the structure function is expected to saturate. However, it could also likely be caused by regular structures, for example, a traveling wave with a wavelength of about twice that of the length at the turnover point (∼ 150 km). The contribution of phase tilt of such a wave to

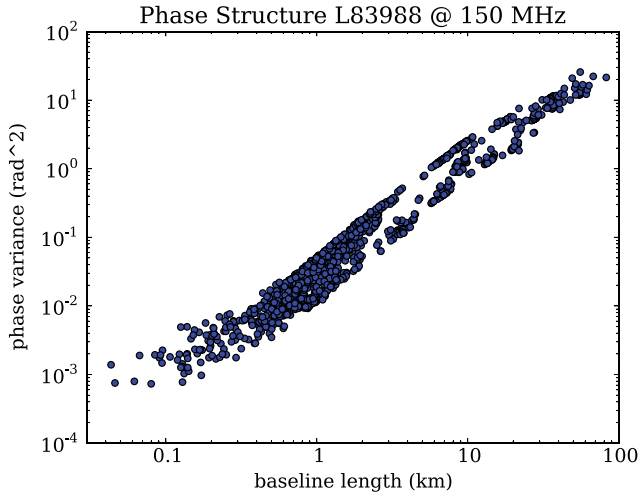

Figure 3. Phase structure function of the same observation as in Figure 2. The differential TEC values are converted to phases at 150 MHz.

the phase structure function would be a power law with power 2.0 [*Wandzura*, 1980], larger than the 5/3 for Kolmogorov turbulence. Inclusion of LOFAR's (longer) international baselines in the analysis will yield an unambiguous measurement of the outer scale, which we have not pursued here.

The turnover at the shorter baseline lengths in Figure 3 is due to the presence of a noise floor. As discussed in section 3, the second-order contributions to the calibration phases, not taken into account during clock/TEC separation, lead to small systematic variations in the fitted TEC values. This can be studied by examining the residuals of the fit of the function in equation (2) to the calibration phases. The time variation of these residuals is shown in Figure 4 for a single baseline and a single subband of a large range of observations. There is a strong correlation between the residuals of different observations, suggesting a common systematic error. Since all observations are aligned in local sidereal time, either the incompleteness of the sky model or beam model errors are good candidates for these residual calibration phases. See, for example, *Wijnholds et al.* [2016] for a more elaborate discussion of the effect of missing flux on calibration errors. For one observation we redid the calibration and clock/TEC fitting with the 10 brightest sources in the field added to the sky model. The resulting

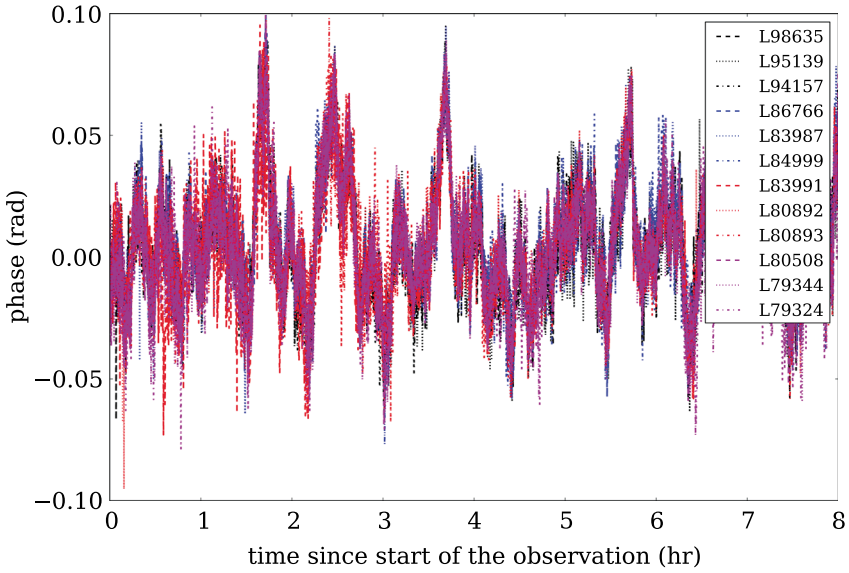

Figure 4. Phase residuals versus time after clock/TEC separation, single subband. The different lines correspond to different observations. There is a striking correlation between the residuals of different observations, suggesting a common cause of systematic errors.

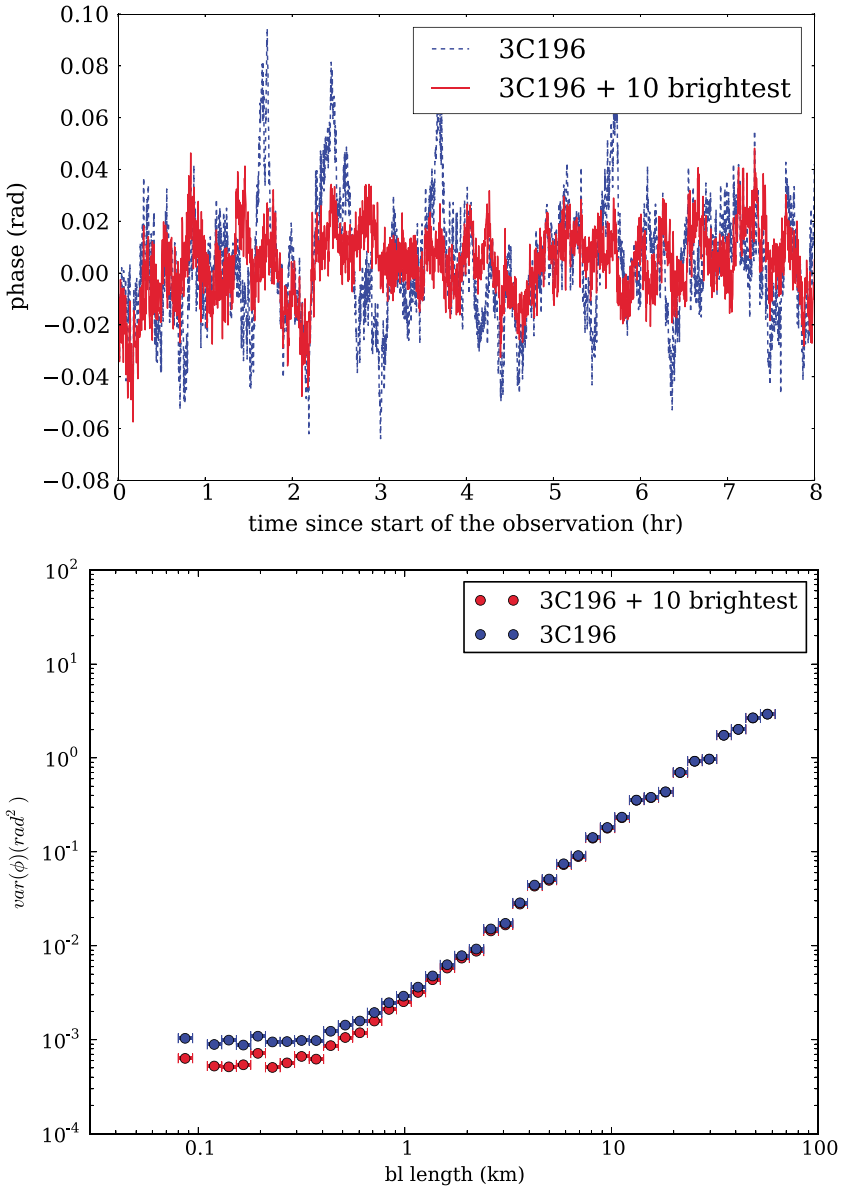

Figure 5. (top) Phase residuals after clock/TEC separation. Comparison of the residuals using a single source model and a more complete sky model with 10 additional sources during calibration. (bottom) Difference in phase structure for the two different sky models. Only the middle 4 h of the observation were taken into account. The noise floor at shorter baselines is about a factor 2 lower for the improved model.

residuals, shown in Figure 5, are indeed smaller and different in structure. We also show in Figure 5 that the noise floor of the phase structure function for this particular observation indeed drops when including more sources in the model, when only the middle 4 h of the observation were used. However, if we include the full 8 h of the observation, we noticed a systematic effect especially at the start and end of the observation, when the elevation angles are lower, that could not be reduced by improving the sky model. This source of systematic noise at low elevations could probably be attributed to an imperfect model of the primary beam. If not properly taken into account, these systematic effects in the phases will lead to small systematic errors in the clock/TEC separation. Assuming that the turnover at the short baselines in the structure function can be completely attributed to these systematic errors, we can estimate the uncertainty on the TEC values from the noise floor. Noise will add an additional term to the phase structure function. We chose to use a single constant term for the noise, although, in principle, the systematic noise could be spatial correlated. To check the validity of this simplification, we measured the structure function of the difference between the independently fitted

TEC of both polarizations, which showed a flat spectrum. The expression for the estimated phase structure becomes

$$D(r) = \left(\frac{r}{r_{\text{diff}}}\right)^{\beta} + \sigma^2, \tag{6}$$

which describes the phase structure for an isotropic medium up to the turnover point at large scales.

Another typical feature of the phase structure function is the band-like structure, of which an example in Figure 3. This structure is seen in many observations and was found to be dependent on the orientation of the baseline. The fact that the phase structure has a different scale (r_{diff}) for different directions, although the slope is more or less equal, suggests that the ionospheric irregularities are anisotropic. Like the turnover point at long baseline lengths, this envelope structure is also consistent with a contribution from large wavelike structures that propagate in the direction where the smallest diffractive scales are measured. The anisotropy of the ionospheric structure has been observed before [*Wheelon*, 2001; *Spencer*, 1955; *Singleton*, 1970]. It can be taken into account in the structure function by making the function two dimensional:

$$E(\mathbf{r}) = (\mathbf{r}^{\top}\mathbf{R}^{\top}\Sigma\mathbf{R}\mathbf{r})^{\beta/2} + \sigma^2 \quad \Sigma = \text{diag}\left(\left(\frac{1}{r_{\text{diff}}^{\text{maj}}}\right)^2, \left(\frac{1}{r_{\text{diff}}^{\text{min}}}\right)^2\right), \tag{7}$$

with $r_{\text{diff}}^{\text{maj}}, r_{\text{diff}}^{\text{min}}$ the diffractive scales of the major and minor axes and $\mathbf{r} = (r_x, r_y)$ the vector of baseline lengths projected on an appropriate orthogonal frame (we chose r_x to be EW and r_y to be NS oriented). $\mathbf{R}$ is the 2×2 rotation matrix of angle α, the orientation of the major axis within this frame (north to east). A qualitative discussion on the anisotropy and its orientation can be found in section 5.3.

We constructed the phase structure function for all observations under consideration and fit for parameters $r_{\text{diff}}^{\text{maj}}, r_{\text{diff}}^{\text{min}}, \alpha, \beta$, and σ in equation (7) to determine the characteristics of the ionosphere. As will be discussed in section 5.2, the diffractive scale is a good candidate to quantify the ionospheric quality of a night with a single number. In order to assign a single measure for the ionospheric quality of the night, we used the simple 1-D function in equation (6) to get an estimate of the average diffractive scale r_{diff}, where, for stability, we fixed the value of β to the result of equation (7) to the data.

The time averaging can lead to systematic errors in the determination of the structure function parameters. Large peaks in the differential TEC values, for example, can have a major impact on the variance. We investigated the systematic errors due to the time averaging in the following way. For each observation we generated five independent subsets with random time sampling. The fit was performed for all subsets, and we calculated the variance of the five values per parameter. These variances were, in general, much larger than the statistical errors from the fit, indicating that there are indeed systematic uncertainties. These standard deviations were quadratically added to the covariance errors from the fit of the full data set to get a conservative estimate of the total uncertainty of the fitted parameters.

5. Results

5.1. Structure Functions Fit

Figures 6 and 7 show the phase structure functions of all 29 observations with the results of the fits superimposed. We summarize our results of the fits described in section 4 in Table 1. Figures 8 a and 8b show histograms of the main characteristics of the ionosphere, namely, the fitted slope β and r_{diff}. We notice that on average the value for β is larger than the pure Kolmogorov value of 5/3. The average value for β is 1.89 with a standard deviation of 0.1. A priori there is no reason that the power index of the ionospheric structures should be exactly 5/3 , which is the value derived for turbulence in the lower atmosphere [*Rufenach*, 1972]. The higher index is likely to be due to nonturbulent structures (for example, traveling ionospheric disturbances (TIDs) [*van Velthoven*, 1990] or density ducts [*Loi et al.*, 2015]) in the ionosphere. The contribution of the wavelike TIDs to the structure function is a power law with power 2.0, which from Figure 8 appears to be the cutoff value for β. Besides, both the turnover at long baselines that is observed in some observations and the orientation dependent band-like structure are also consistent with being caused by large-scale, coherent fluctuations such as medium scale TIDs.

The standard deviation measured from the noise floor is fairly constant per observation and on average 0.9 mTEC. This is the minimal level of accuracy on differential TEC that we can achieve on data of a bright calibrator. Improving the model of the instrument and the sky can further increase the accuracy. The distribution of the diffractive scale r_{diff} values varies between 3 and 30 km.

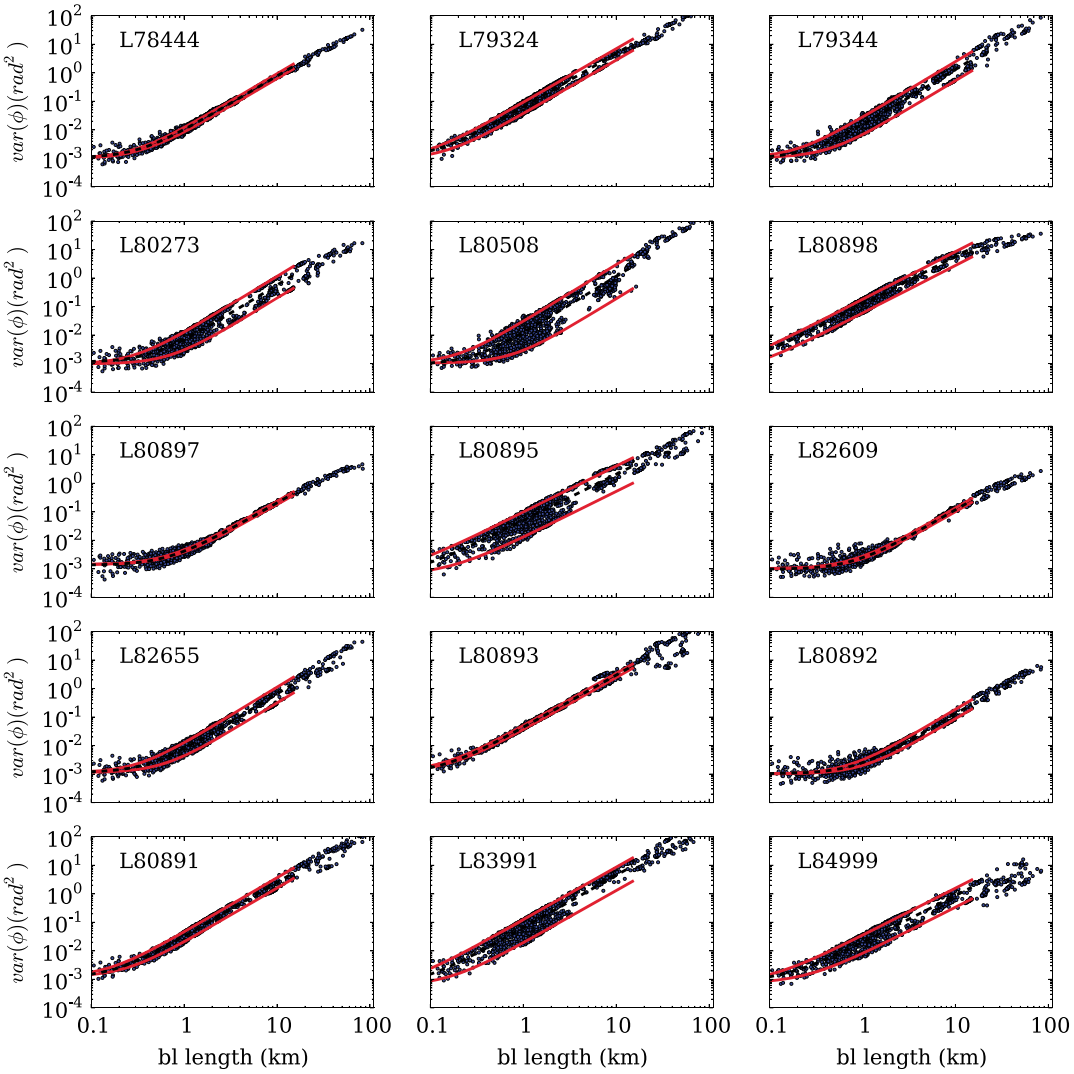

Figure 6. Structure functions of all observations. The lines are the major and minor axis projections of the fitted function (7).

5.2. Diffractive Scale

A small diffractive scale corresponds to large phase fluctuations over the field of view. The time coherence of the signal is shorter for smaller diffractive scales, depending also on the baseline length [*Vedantham and Koopmans*, 2015]. To compensate for these fluctuations, it is needed to calibrate the phases in many directions on short timescales. The number of directions and the time resolution of the solutions is limited by the available source flux and number of independent data points [*Bregman*, 2012]. The r_{diff} appears to be a good measure of the ionospheric quality for radio interferometric imaging of the night. For EoR purposes it was shown in *Vedantham and Koopmans* [2015] that a diffractive scale larger than 5 km at 150 MHz is sufficient. This corresponds to 90% of the observations. In extreme cases, when the diffractive scale becomes smaller than the Fresnel scale (about 300 m at 150 MHz), we get diffractive amplitude and phase scintillations. Such conditions have been observed with LOFAR but not for the observations under consideration. For the observations under consideration we noticed a large night to night variation in the root-mean-square (RMS) image noise of data only calibrated with direction-independent calibration. We measured the image noise as the root-mean-square of the pixel values in source free regions at the edges of the images, where each image was constructed from the calibrated visibilities of a single subband. Interpolation of a polynomial fit on the RMS per frequency resulted in a RMS value at the lower edge of the frequency range, where the ionospheric effects are most severe. For the images the full 8 h data set, if available, was used. To compare observations with different lengths, the measured image noise values were scaled with the square root of the number of visibilities. This

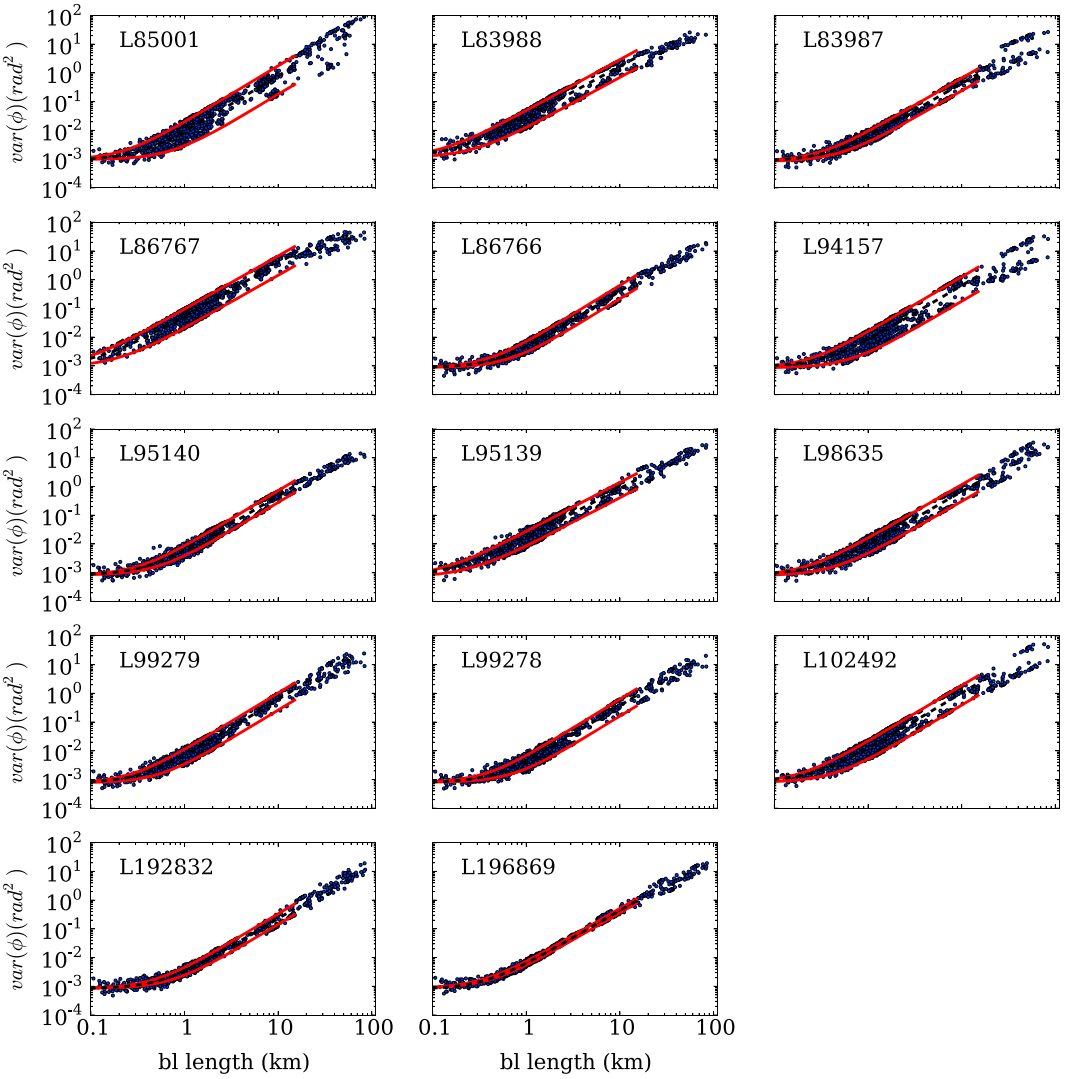

Figure 7. Structure functions of all observations. The lines are the major and minor axis projections of the fitted function (7).

scaling is only approximately correct, since the noise in the images is far from thermal. However, the number of visibilities between different observations differs only by 30% at most, and we only qualitatively investigate the correlation between diffractive scale and image noise, justifying using this approximation here. In order to test if the night to night RMS variation could be explained by variation in the ionospheric conditions, we plotted in Figure 9 the rescaled image RMS versus the measured diffractive scale. The RMS values are rescaled to an arbitrary scale between 0 and 1. Although the scatter is large, there is clear evidence of an inverse correlation between the diffractive scales and image noise. A quantitative analysis and comparison to *Vedantham and Koopmans* [2015], who computed the theoretical residual ionospheric noise after self calibration, is left for future work. Figure 9 is merely an illustration of the anticorrelation between image noise and diffractive scale; therefore, the RMS values are rescaled to an arbitrary scale between 0 and 1.

5.3. Anisotropy

We investigated the level of anisotropy in the ionospheric structure as well as the angle of the major axis with respect to the north Meridian. The level of anisotropy, i.e., ratio of the major and the minor axis, in Table 1 ranges from 1 to 4. Earlier observations [*Spencer*, 1955; *Singleton*, 1970; *Wheelon*, 2001] suggest that the ionospheric irregularities are aligned and elongated along the Earth magnetic field lines, which would result in a larger diffractive scale for the field-aligned baselines. Taking into account the viewing direction in the direction of 3C196, one gets a perspective view of the magnetic field lines when projected on a given ionospheric

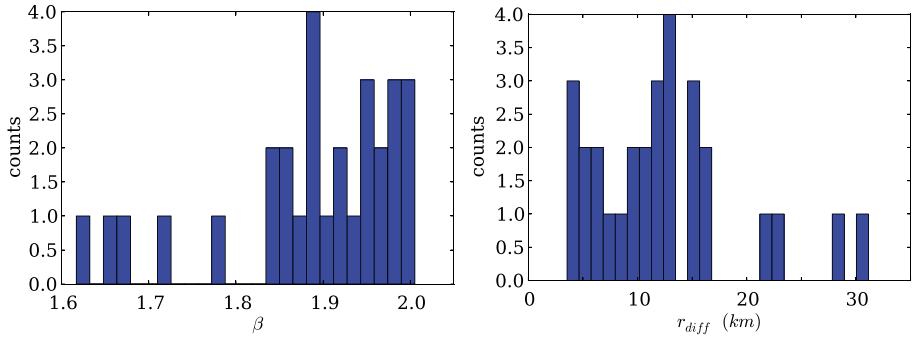

Figure 8. (left) Histogram of measured values for β. (right) Histogram of measured values for diffractive scale r_{diff}.

altitude. This method of projecting the field lines is discussed in *Loi et al.* [2015]. Since the angle of the baseline with respect to the projected magnetic field lines changes with time, a single variance per baseline cannot be calculated anymore. Instead, after removing a global trend per baseline, the TEC data were binned in two-dimensional angle and length bins. We removed the global trend explicitely, where before it was done implicitly by making use of the phase variance, since different baselines contribute to the same bin. We used the World Magnetic Model for modeling the magnetic field lines [*Chulliat et al.*, 2014]. An example of the variance per bin for a single observation, in which the observed field-aligned anisotropy was high, is shown in Figure 10. For many, but not all, observations that do show anisotropy, the ionospheric irregularities seem to be indeed elongated along the magnetic field lines, with relative differences in diffractive scale in the field aligned and perpendicular direction up to a factor 6. In the last column of Table 1 we give the ratio of the field aligned and perpendicular diffractive scales. For about 60% of the observations this ratio is larger than 2, indicating some field-aligned irregularities. This correlation with the magnetic field could well be related to the *density ducts* as observed by *Loi et al.* [2015]. Their observations show elongated field-aligned structures that move with low speeds. If such structures were present during the observations under consideration, they would indeed lead to similar structure functions.

Another contributor to the observed anisotropy could be medium size traveling ionospheric disturbances (mTIDs) [*van Velthoven*, 1990]. TIDs are, in general, not field aligned, but they could well be the explanation for those observations that do show anisotropy, but for which the anisotropy is not field aligned. Baselines that are parallel to the wavefront of such waves are insensitive to their contribution to the phase structure. The structure function of a single wave has a slope of 2.0 until the turnover point around half a wavelength. Since no significant turnover is observed below 80 km, the wavelengths of these waves have to be larger than 150 km. The observed anisotropies would correspond to amplitudes of the waves of the order of 0.1 – 0.5 TECU, depending on the level of anisotropy and the assumed wavelength. These values are consistent with typical

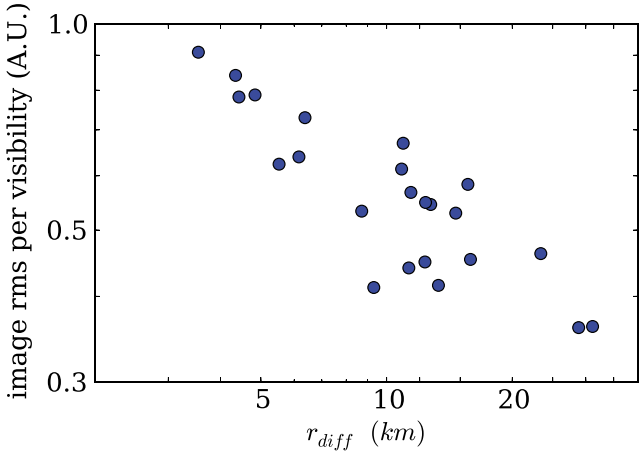

Figure 9. Image RMS versus measured diffractive scale. The image RMS was scaled with $\sqrt{\#\text{ visibilities}}$ and calculated after one round of direction independent self calibration using a four component model of the central source only.

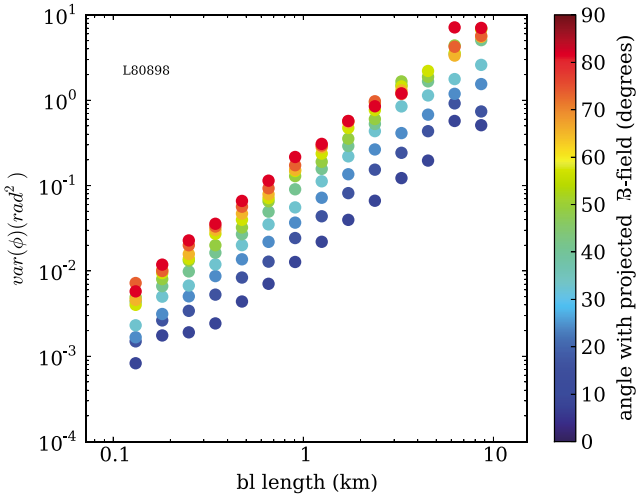

Figure 10. Phase structure function of a single observation, with the data binned according to the angle with respect to the projected Earth magnetic field, given in radians with the color bar. The diffractive scale is evidently smaller; thus, the points are higher, for perpendicular baselines in comparison to the parallel.

amplitudes and wavelengths of mTIDs [*van Velthoven*, 1990]. This is also in agreement with the distribution of values for β, which appear to cutoff at a value of 2.0. In this case, the angle of the major axis of the two-dimensional structure function gives an indication of the traveling direction of such waves. The angles of the major axes with respect to the north meridian are plotted in Figure 11. The closed arrows correspond to the observations where no correlation with the magnetic field was observed, i.e., where the ratio of the field aligned and perpendicular diffractive scales was smaller than 2. The open arrows denote the observations where field aligned structures were present. It should be stressed, however, that the vectors are calculated using the original 2-D structure functions, so without using the Earth magnetic field projection. In this plot the length of the vectors is determined by the level of anisotropy minus 1: $r_{\mathrm{diff}}^{\mathrm{maj}}/r_{\mathrm{diff}}^{\mathrm{min}} - 1$, such that a zero length vector corresponds to no anisotropy. We do not observe a preferred direction of the anisotropy of the non–field-aligned structures.

The fact that the ionospheric structures are anisotropic with the irregularities in many cases geomagnetically aligned, probably has minor impact on the original purpose of our research, namely, investigating calibration strategies and estimating noise characteristics. However, the two different diffractive scales need be taken into account in the calculations of estimated noise. Also, a model of the ionosphere for calibration purposes, e.g., with a method like SPAM [*Intema et al.*, 2009], could benefit from the knowledge that the structures are field-aligned structures and thus tilted with respect to the Earth's surface.

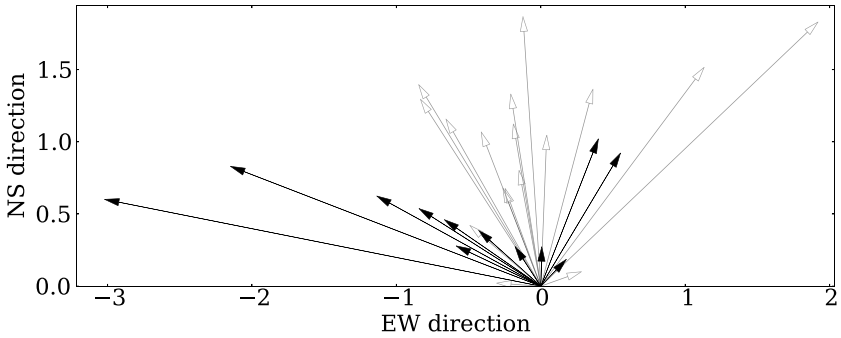

Figure 11. Direction and size of anisotropy for all observations. Closed arrows: observations that do not show Earth magnetic field aligned structures. Open arrows: observations that have a field-aligned structure ratio of at least 2. The length of the vectors is defined as $r_{\mathrm{diff}}^{\mathrm{maj}}/r_{\mathrm{diff}}^{\mathrm{min}} - 1$.

6. Conclusion

We have shown that LOFAR is able to measure with an accuracy better than 1 mTEC the differential TEC values on spatial scales between 1 and 100 km, when using the calibration phases with a time resolution of 10 s in the direction of a bright calibrator. Using a better sky and instrument model during calibration could improve this accuracy.

We measured the spatial phase structure above LOFAR of many nights in the winters of 2012/2013 and 2013/2014. We observed a power law behavior over a long range of baseline lengths, between 1 and 80 km. The average slope is 1.89 with a one standard deviation spread of 0.1, in general, larger than the 5/3 expected for Kolmogorov turbulence. In some observations, we have tentatively detected a turnover in the phase structure function at baseline lengths larger than 80 km. Both the turnover and the large β values are an indication of the contribution of coherent fluctuations, like, for example, traveling waves, to the structure function.

There is a large night-to-night variation of the diffractive scale, which directly translates into image noise variation, if the directional dependence of the ionospheric distortion is not properly accounted for in the calibration. Therefore, the diffractive scale could serve as a measure of the ionospheric quality of an observation. Theoretical predictions of the expected image noise dependence on ionospheric diffractive scales are discussed in *Vedantham and Koopmans* [2015]. When minimal residual noise is required, such as for the LOFAR EoR project, it is important to assign an ionospheric quality in order to decide which observations are useful. The measured diffractive scales at 150 MHz range between 3 and 30 km. *Vedantham and Koopmans* [2015] have argued that for the LOFAR EoR measurement a minimal r_{diff} of 5 km is needed. This is the case for 90% of the observations discussed here. Furthermore, for the generation of a sky model used in subsequent direction dependent calibration, only the best nights, with a $r_{\mathrm{diff}} > 20$ km, are used, such that image distortion at the highest resolution is minimal.

We observed an anisotropy ratio of the ionospheric structure ranging between 1 (no anisotropy) and 6, that is, in many, but not all, cases aligned along the Earth magnetic field. The field-aligned anisotropy is reminiscent of the observations of large field-aligned structures in *Loi et al.* [2015]. If not Earth magnetic field aligned, the observed anisotropy could again also be explained by a contribution from traveling waves, where the shortest diffractive scales are measured along the wave propagation direction.

It should be noted that the results discussed here only consider nighttime data. Ionospheric effects during daytime and sunrise and sunset are expected to be different due to the solar irradiation. Also, all observations were done in wintertime. It is likely that seasonal variations have an effect on the ionospheric structure function.

Acknowledgments
This research was supported by grants from the Netherlands Organization for Scientific Research (TOP grant 614.001.005) and from the European Research Council (grant 339743 (LOFARCORE)). All data presented here are made available upon request by the corresponding author.

References

Bregman, J. D. (2012), System design and wide-field imaging aspects of synthesis arrays with phased array stations: To the next generation of SKA system designers, PhD Thesis, Groningen Univ. [Available at http://www.rug.nl/research/portal/publications/pub(b3999be9-f783-4d2c-aa56-c172ac8e51c8.]

Chulliat, A., S. Macmillan, P. Alken, C. Beggan, M. Nair, B. Hamilton, A. Woods, V. Ridley, S. Maus, and A. Thomson (2014), *The US/UK World Magnetic Model for 2015-2020*,NOAA National Geophysical Data Center, Boulder, Colo., doi:10.7289/V5TH8JNW.

Cohen, A. S., and H. J. A. Röttgering (2009), Probing fine-scale ionospheric structure with the very large array radio telescope, *Astron. J.*, *138*(2), 439–447, doi:10.1088/0004-6256/138/2/439.

Cotton, W. D., et al. (2004), Beyond the isoplanatic patch in the VLA low-frequency sky survey, *Proc. SPIE*, *5489*, 180–189, doi:10.1117/12.551298.

Helmboldt, J. F., T. J. W. Lazio, H. T. Intema, and K. F. Dymond (2012), A new technique for spectral analysis of ionospheric TEC fluctuations observed with the Very Large Array VHF system: From QP echoes to MSTIDs, *Radio Sci.*, *47*, RS0L02, doi:10.1029/2011RS004787.

Intema, H. T., S. van der Tol, W. D. Cotton, A. S. Cohen, and H. J. A. Röttgering (2009), Ionospheric calibration of low frequency radio interferometric observations using the peeling scheme, *Astron. Astrophys.*, *501*(3), 1185–1205, doi:10.1051/0004-6361/200811094.

Jacobson, A. R., and W. C. Erickson (1992), A method for characterizing transient ionospheric disturbances using a large radiotelescope array, *Astron. Astrophys.*, *257*, 401–409.

Koopmans, L. V. E (2010), Ionospheric power-spectrum tomography in radio interferometry, *Astrophys. J.*, *718*, 963–971, doi:10.1088/0004-637X/718/2/963.

Loi, S. T., et al. (2015), Real-time imaging of density ducts between the plasmasphere and ionosphere, *Geophys. Res. Lett.*, *42*, 3707–3714, doi:10.1002/2015GL063699.

Loi, S. T., et al. (2015), Power spectrum analysis of ionospheric fluctuations with the Murchison Widefield Array, *Radio Sci.*, *50*, 574–597, doi:10.1002/2015RS005711.

Narayan, R. (1992), The physics of pulsar scintillation, *Philos. Trans. R. Soc. A*, *341*(1660), 151–165, doi:10.1098/rsta.1992.0090.

Offringa, A. R., A. G. de Bruyn, M. Biehl, S. Zaroubi, G. Bernardi, and V. N. Pandey (2010), Post-correlation radio frequency interference classification methods, *Mon. Not. R. Astron. Soc.*, *405*(1), 155–167, doi:10.1111/j.1365-2966.2010.16471.x.

Offringa, A. R., et al. (2012), The LOFAR radio environment, *Astron. Astrophys.*, *539*, A95, doi:10.1051/0004-6361/201220293.

Pandey, V. N., J. E. van Zwieten, A. G. de Bruyn, and R. Nijboer (2009), *Low-Frequency Radio Universe, Astron. Soc. of the Pacific Conf. Ser.* edited by D. J. Saikia et al., pp. 384–388, Astron. Soc. Pacific, San Francisco, Calif.

Pearson, T. J., and A. C. S. ReadHead (1984), Image formation by self-calibration in radio astronomy, *Ann. Rev. Astron. Astrophys.*, *22*, 97–130, doi:10.1146/annurev.aa.22.090184.000525.

Rufenach, C. L. (1972), Power-law wavenumber spectrum deduced from ionospheric scintillation observations, *J. Geophys. Res.*, *77*, 4761–4772, doi:10.1029/JA077i025p04761.

Singleton, D. G. (1970), Dependence of satellite scintillations on zenith angle and azimuth, *J. Atmos. Terr. Phys.*, *32*(5), 789–803, doi:10.1016/0021-9169(70)90029-2.

Smirnov, O. M. (2011), Revisiting the radio interferometer measurement equation I. A full-sky Jones formalism, *Astron. Astrophys.*, *527*, A106, doi:10.1051/0004-6361/201016082.

Spencer, M. (1955), The shape of irregularities in the upper ionosphere, *Proc. Phys. Soc. B*, *68*(8), 493–503, doi:10.1088/0370-1301/68/8/302.

Spoelstra, T. A. Th. (1997), The ionosphere and radio interferometry, *Ann. Geophys.*, *40*(4), 865–914, doi:10.4401/ag-3885.

van der Tol, S. (2009), Bayesian estimation for ionospheric calibration in radio astronomy, PhD Thesis, Delft Univ. of Technol., Delft, Netherlands.

van Haarlem, M. P., et al. (2013), LOFAR: The LOw-Frequency ARray, *Astron. Astrophys.*, *556*, A2, doi:10.1051/0004-6361/201220873.

van Velthoven, P. F. J. (1990), Medium scale irregularities in the ionospheric electron content, PhD Thesis, Eindhoven Univ., Netherlands.

Vedantham, H. K., and L. V. E Koopmans (2015), Scintillation noise in widefield radio interferometry, *Mon. Not. R. Astron. Soc.*, *453*, 925–938, doi:10.1093/mnras/stv1594.

Wandzura, S. M. (1980), Meaning of quadratic structure functions, *J. Opt. Soc. Am.*, *70*(6), 745–747, doi:10.1364/JOSA.70.000745.

Wheelon, A. D. (2001), *Electromagnetic Scintillation, Geometrical Optics*, vol. 1, Cambridge Univ. Press., doi:10.1017/CBO9780511534805.

Wijnholds, S. J., T. L. Grobler, and O. M. Smirnov (2016), Calibration artefacts in radio interferometry—II. Ghost patterns for irregular arrays, *Mon. Not. R. Astron. Soc.*, *457*(3), 2331–2354, doi:10.1093/mnras/stw118.